Hybrid density functional theory study of vanadium doping in stoichiometric and congruent $LiNbO_3$

Yongjun Fan,[1] Lili Li,[1] Yanlu Li,[1,*] Xueqin Sun,[2,†] and Xian Zhao[1,‡]

[1]*State Key Lab of Crystal Materials and Institute of Crystal Materials, Shandong University, Jinan 250100, China*

[2]*School of Environmental and Material Engineering, Yantai University, Yantai 264005, China*

(Received 13 July 2018; revised manuscript received 11 December 2018; published 23 January 2019)

The basic features of vanadium (V)-doped $LiNbO_3$, such as V doping sites, local lattice distortions, and electronic structures are investigated via hybrid density functional theory. The interaction between V and the intrinsic point defects is also studied in this work. V is found to prefer to substitute Li (V_{Li}) at its highest charge state of +4 in most $LiNbO_3$ samples, and begins to substitute Nb to form a neutral V_{Nb} defect as the Fermi level is increased. Furthermore, V_{Li} exhibits different polaronic behaviors in stoichiometric and congruent $LiNbO_3$. The most stable V_{Li}^{4+} tend to form a V_{Li}^{2+} small bound polaron by simultaneously capturing two electrons in stoichiometric $LiNbO_3$, and form a bound bipolaron along the nonpolarization axis in the congruent samples. Moreover, both bound bipolarons along the polarization and nonpolarization axes are found in congruent $LiNbO_3$ by capturing two more electrons.

DOI: 10.1103/PhysRevB.99.035147

I. INTRODUCTION

Lithium Niobate ($LiNbO_3$) is a multifunctional material [1], with prominent ferroelectric, electro-optical, piezoelectric, photorefractive characteristics [2], and has broad applications in piezoelectric sensors, second harmonic generators, holographic storage, surface acoustic wave devices, etc. [3–5]. It has been well demonstrated that $LiNbO_3$ can be modified to suit a specific application by controlling the extrinsic and intrinsic defect structures in crystal through doping and composition modification [6–11]. For instance, dopants such as Fe, Cu, Mn, and Ce can improve the photorefractive ability of $LiNbO_3$ [12,13], since they possess the ability to provide or capture d or f electrons to generate defect levels in the band gap. We notice that most of these dopants own valence states that are lower than Nb (i.e., the intrinsic photorefractive center Nb_{Li}). In principle, dopants with higher valence states have lower formation energies and stronger electron capture ability than the dopants with lower valence states, thereby affording them interesting photorefractive properties.

Kong's group has recently successfully grown vanadium (V)-doped $LiNbO_3$, which has much faster photorefractive response speed and higher sensitivity than the commonly used Fe-doped $LiNbO_3$ [6,7]. However, there are some fundamental problems with V-doped $LiNbO_3$, such as the fact that the preferable substitution site, stable charge state, and defect state property have yet to be elucidated. The study of the structure, stability, and electronic structure is essential to further understand the doping-induced optical properties of $LiNbO_3$. It is well known that the antisite Nb_{Li}^{4+} can introduce small bound polarons and bipolarons in $LiNbO_3$ by capturing one and two electrons, respectively [14–16]. Since V^{5+} has the same valence state as Nb^{5+}, it is of particular interest to learn the electron self-trapping and polaronic behavior of V-doped $LiNbO_3$. In addition, $LiNbO_3$ grown via the Czochralski technique [17–20] are normally Li-deficient and prone to various intrinsic defects, such as the antisite Nb_{Li} and Li vacancy Vac_{Li}^{-}, which are widely referred to as congruent $LiNbO_3$ [5,21–25]. The interaction between V and these intrinsic defects is another important characteristic that should be understood. The existence of the intrinsic defects could lead to large lattice relaxation and charge distribution around the dopant, and thus the variable V-doping behavior in stoichiometric and congruent $LiNbO_3$. However, related experimental and theoretical research has not yet been reported.

In this work, the defect formation energies, lattice distortions, and electronic structures of V-doped $LiNbO_3$ were investigated by using the density functional theory (DFT) [26,27]. The typically used (semi)local functional consistently underestimates the band gaps of semiconductors [28], which consequently significantly affects the predictive power of approximation when applied to defect levels [29,30], especially with respect to the highly localized d states of Nb and V, where strong correlation occurs [31,32]. Therefore, in this study, the spin-polarized hybrid functional [33,34] was used to investigate the lattice distortion, energetics, and electronic structure of V-doped $LiNbO_3$. Additionally, the interaction of V dopant with the intrinsic defect Nb_{Li} was investigated and the configurations and energetics of charge-compensated defect clusters were investigated by using (semi)local functionals in order to minimize computational cost.

II. COMPUTATIONAL DETAILS

In this study, the Vienna *ab initio* Simulation Package (VASP) [35,36] implementation of DFT is employed in

*Author to whom correspondence should be addressed: liyanlu@sdu.edu.cn

†sxq@ytu.edu.cn

‡xianzhao@sdu.edu.cn

conjunction with the projector-augmented-wave (PAW) formalism [37] to perform calculations. Thereby the Li $2s^1$, Nb $4p^6 4d^4 5s^1$, O $2s^2 2p^4$, and V $3d^3 4s^2$ states are treated as valence electrons. The electron wave function is extended by an energy cutoff of 400 eV. Isolated V-substituting Li (V_{Li}) and V substituting-Nb (V_{Nb}) are modeled with cells of different sizes. Hexagonal supercells containing 240 atoms are implemented in the energetic calculations within the DFT-GGA (DFT-generalized gradient approximation). Therefore, the Perdew, Burke, and Ernzerhof (PBE) [38] functional is used to model the electron exchange-correlation energy within the GGA. All lattice constants and atomic positions are optimized for all supercells, and the force convergence criterion for the structural relaxation is set as 0.01 eV/Å. Smaller hexagonal supercells containing 120 atoms are also implemented in the electronic structure calculations by utilizing the Hyde-Scuseria-Ernzerhof (HSE06) screened hybrid functional [33,34]. In this approach, the long-range exchange potential and correlation potential are calculated by using the DFT-PBE functional, and the short-range exchange potential is calculated by mixing a fraction of the nonlocal Hartree-Fock exchange with DFT-PBE. We tested the band gap of pristine $LiNbO_3$ by changing the fraction of the exact exchange from 0.15 to 0.35 in 0.05 intervals. It is found that when the fraction of exact exchange equals 0.25 (the standard value), the calculated band gap is closest to the value of 5.37 eV which was previously obtained via the more accurate G_0W_0@GGA method [8]. Considering this, the screening length and mixing parameter are fixed at 10 Å and 0.25, respectively. The spin polarization of the V $3d$ shell is considered in the structural optimization, energetic, and electronic structure calculations for the isolated V_{Li} and V_{Nb} defects. Therefore, the formation energies of single V-doped $LiNbO_3$ are calculated within spin-polarized DFT. The electronic structures of single V-doped $LiNbO_3$ are performed based on the supercells optimized by spin-polarized HSE06 functional in order to accurately describe the local lattice distortions, energetics, and the electronic structures of V high-spin states. Most of the defect pairs and defect clusters are modeled in 360- and 540-atom supercells within DFT-PBE in order to minimize the computational cost with the exception of the electronic structure calculations for defect pairs, which are calculated by using hybrid functional. $4 \times 4 \times 4$, $4 \times 4 \times 4$, and $2 \times 2 \times 2$ Monkhorst-Pack k-point meshes [39] are implemented in the DFT-PBE calculations of 120-, 240-, and 360-atom supercells respectively; Γ point is implemented in the DFT-PBE calculations of 540-atom supercells and HSE06 calculations of 120-atom supercells.

The defect formation energies of the dopant with q charge state that is dependent on the Fermi level position are calculated as follows [40,41]:

$$E_f(X^q) = E^{\mathrm{tot}}(X^q) - E^{\mathrm{tot}}(\mathrm{bulk}) - \sum_i n_i \mu_i + q(E_F + E_v) - q\Delta V_{0/\mathrm{b}} + E_{\mathrm{corr}}, \quad (1)$$

where $E^{\mathrm{tot}}(X^q)$ and E^{tot} (bulk) are the total energies obtained from a supercell with and without the doping ion X with a charge state q. n_i represents the number of atoms of species i that have been added or removed during doping, and μ_i are the corresponding chemical potentials. E_F is the Fermi level with respect to the bulk valence band maximum (VBM) E_v, and $\Delta V_{0/\mathrm{b}}$ is a term to align the potential of the bulk and the defective supercells. This term could be obtained by comparing the electrostatic potentials between the bulk-like region far from the neutral defect and the bulk: $\Delta V_{0/\mathrm{b}} = V_{0|\mathrm{far}} - V_{\mathrm{b}}$ [42]. E_{corr} is an electrostatic correction that was developed by Freysoldt, Neugebauer, and Van de Walle [43,44] to account for the finite-size supercell error. It is suitable for the case of charged defects within a dielectric medium. Following Ref. [45], the correction is expressed as

$$E_{\mathrm{corr}}^{\mathrm{FNV}} = E_{\mathrm{lat}} - q\Delta V_{q/0}\,. \quad (2)$$

In the case of the point-charge model that was implemented in this study, the lattice energy E_{lat} corresponds to the first item of the Makov-Payne expression for the electrostatic correction [43,46], as follows:

$$E_{\mathrm{corr}}^{\mathrm{MP}} = \frac{q^2 \alpha_M}{2\varepsilon_s L} + \frac{2\pi q Q}{3L^3 \varepsilon_s} + O\,(L^{-5}), \quad (3)$$

where q is the total charge, Q is the quadrupole moment of the defect-induced charge, α_M is the Madelung constant, ε_s is the static bulk permittivity, and L is the linear size of the supercell. Because the $LiNbO_3$ is a typical polar crystal, its experimental static dielectric tensor component values tend to be highly anisotropic ($\varepsilon_s^{11} = 84$ and $\varepsilon_s^{33} = 29$) [47]. Therefore, the weighted average of experimental ε_s^{11} and ε_s^{33} are used in order to avoid the larger calculation error associated with using only one component. Thus, a weighted average based on the ratio of the a and c lattices would be preferable to the normal averaging strategy because the polarization factor is introduced to the value of the static dielectric constant. The calculated Freysoldt correction differences by two averaging strategies (weighted and normal) are 0.14 eV to the maximum, and this could not influence the relative stability of the defects. The second item $\Delta V_{\mathrm{q/0}}$ corresponds to the potential alignment by taking the neutral defect model as a reference.

The chemical potentials μ_i are dependent on the preparation conditions. The thermodynamic considerations restrict the accessible range of μ_i, if there is $LiNbO_3$ stability, which is the stability of the ternary compound $LiNbO_3$ against decomposition into its single component constraints and its binary oxides Li_2O and Nb_2O_5 [48,49]. We define $\Delta\mu$ as the discrepancy with the bulk values of the chemical potential of the corresponding component. The stoichiometric sum of the $\Delta\mu_i$ should be equal to the formation enthalpy of $LiNbO_3$,

$$\Delta\mu(\mathrm{Li}) + \Delta\mu(\mathrm{Nb}) + 3\Delta\mu(\mathrm{O}) = -\Delta H_f^{\mathrm{LiNbO_3}}. \quad (4)$$

The thermodynamically stable region is limited to the two extremes of $LiNbO_3$, which is in equilibrium with Li_2O and Nb_2O_5, respectively [48,50]. They can be described as

$$2\Delta\mu(\mathrm{Li}) + \Delta\mu(\mathrm{O}) = -\Delta H_f^{\mathrm{Li_2O}}, \quad (5)$$

$$2\Delta\mu(\mathrm{Nb}) + 5\Delta\mu(\mathrm{O}) = -\Delta H_f^{\mathrm{Nb_2O_5}}. \quad (6)$$

These requirements obtained within DFT-PBE and HSE06 functionals are shown in Fig. 1. The triangle ADG yields the formation enthalpy of $LiNbO_3$ in Eq. (4). The triangle BDF

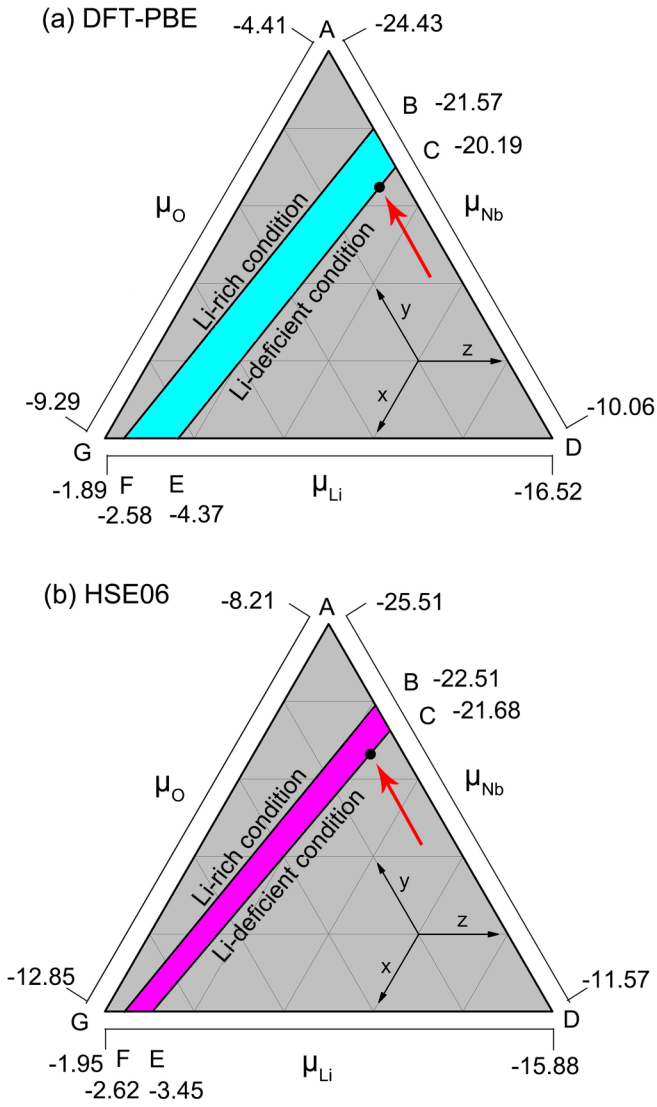

FIG. 1. Stability range of the chemical potentials (in eV) of the $LiNbO_3$ constituents within DFT-PBE (a) and HSE06 (b) functionals respectively. The colored region is the intersection between them and represents the thermodynamically allowed range of the chemical potentials. The arrows point to the black dots that indicate the chemical potentials we used in this work.

and the region enclosed between points A, C, E, and G are defined by Eqs. (5) and (6). Therefore, the shaded region enclosed by BCEF indicates the $LiNbO_3$ stability range, and the values outside of this region lead to the precipitation of the second phases. Furthermore, choosing a different reference state will modify the relative stability of the investigated defects. The calculated chemical potentials of the components by DFT-PBE and HSE06 under Li-rich (line BF) and Li-deficient (line CE) conditions are listed in Table I. Here, we model the defects by using the Nb_2O_5 reference state (line CE) because even nearly stoichiometric $LiNbO_3$ are still Li deficient. The used chemical potentials of each component are also labeled in Fig. 1. In order to ensure that the experimental conditions [6,7] do not change, the chemical potential of V should satisfy the requirement of forming its oxide V_2O_5. This

TABLE I. Calculated chemical potentials (in eV) of Li, Nb, O, and V by DFT-PBE and HSE06 under Li-rich and Li-deficient conditions.

Condition	Component	DFT-PBE	HSE06
Li-rich	Li	− 2.58	− 1.95
	Nb	− 21.57	− 22.51
	O	− 5.06	− 9.21
	V	− 16.32	− 16.56
Li-deficient (congruent $LiNbO_3$)	Li	− 4.37	− 3.45
	Nb	− 20.19	− 21.68
	O	− 4.92	− 8.99
	V	− 16.66	− 17.11

relation is given as

$$2\Delta\mu(\mathrm{V}) + 5\Delta\mu(\mathrm{O}) = -\Delta H_f^{\mathrm{V_2O_5}}. \quad (7)$$

Strictly speaking, in the above equations, the Gibbs free energy should be used to determine the chemical potentials instead of the enthalpy. However, it is customary to replace $G(p, T)$ with the enthalpy, as the entropic terms are expected to be of the same order of magnitude for all of the investigated systems, as explained in detail in Ref. [48] (and references therein). Neglecting the entropy term may thus not qualitatively influence our main conclusion.

The binding energy of the X_1X_2 defect pair is defined as the energy required to separate it into individual defects X_1 and X_2; the calculation formula is shown below:

$$E_c[(X_1X_2)^q] = E_f[(X_1X_2)^q] - E_f\left(X_1^{q_1}\right) - E_f\left(X_2^{q_2}\right), \quad (8)$$

where $q = q_1 + q_2$, and the negative binding energy corresponds to stable defect pairs.

III. RESULTS AND DISCUSSION

A. Defect formation energies

As mentioned above, the point defects simulated by employing the supercell method within the DFT framework are affected by the limited size problem and the unfavorable electronic structure predicted by the local exchange-correlation potential. In this study we separately addressed the effects of these two problems as was discussed in Ref. [15]. First, we performed the Freysoldt correction on the defect formation energies of the 240-atom supercells calculated by the spin-polarized DFT-PBE. Then, we added the exchange-related error to the defect formation energies to obtain accurate defect formation energy results.

First, we estimate the exchange-related error of the defect formation energy calculations. We found that the hybrid functional could significantly improve the description of the $LiNbO_3$ electronic structure [15]. We also compare the calculated formation energies of V_{Li} and V_{Nb} for various possible charge states (i.e., according to electron capture) by using DFT-PBE and HSE06 functionals in 240-atom supercells and the results are presented in Table II. It can be seen that the calculated defect formation energies obtained via the hybrid DFT exhibit energy changes that are several electron

TABLE II. Comparison of the defect formation energies (in eV) of V_{Li} and V_{Nb} obtained within HSE06 and DFT-PBE. Li-deficient conditions suitable for congruent $LiNbO_3$ are chosen.

Defects	E_F (HSE06)	E_F (DFT-PBE)	ΔE_F (HSE06-PBE)
V_{Li}^{4+}	$-8.08+4E_F$	$-3.54+4E_F$	-4.54
V_{Li}^{3+}	$-4.88+3E_F$	$-1.30+3E_F$	-3.57
V_{Li}^{2+}	$-2.02+2E_F$	$1.38+2E_F$	-3.40
V_{Li}^{+}	$2.59+E_F$	$4.35+E_F$	-1.76
V_{Li}^{0}	6.88	7.44	-0.56
V_{Nb}^{0}	-1.67	-1.14	-0.53
V_{Nb}^{-}	$2.20-E_F$	$1.61-E_F$	0.59
V_{Nb}^{2-}	$5.87-2E_F$	$4.65-2E_F$	1.22

volts higher than those calculated by DFT-PBE. Generally, HSE06 gets lower defect formation energies than DFT-PBE (~0.5 eV) for neutral V_{Li} and V_{Nb}; however, the local functional overestimates the defect formation energies of charged V_{Li} defects, and underestimates the defect formation energies of charged V_{Nb} defects. The absolute values of the deviation between the defect formation energies calculated by HSE06 and DFT-PBE are found to increase as the absolute charge of the defects increases. This phenomenon indicates that the electronic self-interaction plays a major role, and that the strongly localized V *d* states are poorly described by the local functional. Assuming that the error generated by using the local functional is mainly related to the orbital characteristics of the defect states and its energy position rather than the supercell size, the nonlocal exchange correction should be defined as the difference between the defect formation energies calculated by HSE06 and DFT-PBE.

The finite-size error is corrected by adding the Freysoldt correction to the defect formation energies calculated by spin-polarized DFT-PBE. Assuming that the defect formation energies with the Freysoldt correction do not take into account the influence of the nonlocal exchange-correlation functional, the approximate defect formation energies, including both previously mentioned effects, can be calculated by incorporating the previously defined exchange correction and Freysoldt correction into the spin-polarized DFT-PBE results by using 240-atom supercells. The final results are shown in Fig. 2. It can be seen that V prefers to substitute a Li site at the +4 charge state when the Fermi energy is near the VBM. As the Fermi energy increases, V_{Li}^{4+} transfers to the +2 charge state by simultaneously capturing two electrons when $E_F = 2.90$ eV, indicating that V_{Li}^{3+} is metastable. The thermodynamic transition level $\varepsilon(3+/2+)$ is found to be located at 2.48 eV, which is lower than that of $\varepsilon(4+/3+)$ (3.33 eV). This switching order of the charge transition levels is indicative of a negative *U* effect [48,49], which is usually associated with large lattice relaxation during electron capture. It is noted that the inclusion of spin polarization in the structural optimizations and energetic calculations could significantly lower the total energies of the systems with nonzero total spin *S*, such as V_{Li} defects with $+3(S=1/2)$ and $+2(S=1)$ charge states, and they are thus more stabilized with respect to the diamagnetic state V_{Li}^{4+} $(S=0)$. However, the total energy

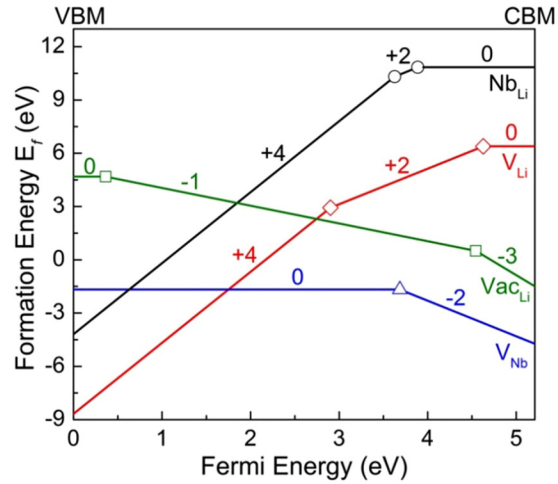

FIG. 2. Defect formation energies of V_{Li} and V_{Nb}, as well as the intrinsic defects Nb_{Li} and Vac_{Li} as a function of the Fermi energy. The Fermi energy range corresponds to the calculated fundamental band gap of $LiNbO_3$, which is 5.21 eV. Li-deficient conditions suitable for congruent $LiNbO_3$ are chosen.

of V_{Li}^{2+} is lowered by 0.89 eV, which is a little bit more than that of V_{Li}^{3+} (0.62 eV). Therefore, spin polarization does not cause the switching of order of $\varepsilon(4+/3+)$ and $\varepsilon(4+/2+)$, and the formation energies of V_{Li} defects still exhibit a negative *U* effect. By capturing two additional electrons, V_{Li}^{2+} directly transfers to V_{Li}^{0} near the conduction band minimum (CBM). Since the Fermi level lies in the lower half of the band gap in realistic $LiNbO_3$ crystals [15], only the +4 and +2 charged V defects are stable at the Li site. The experiments [6,7] also confirmed the presence of V_{Li}^{4+} and V_{Li}^{2+} defects. By comparing the results of V_{Li} and Nb_{Li}, we found that their switching orders of the charge transition levels are the same, but the value of $\varepsilon(4+/2+)$ for V_{Li} is smaller than that for Nb_{Li}, indicating that the V_{Li} defect has stronger electron capture ability than the antisite Nb_{Li}. In the case of V_{Nb}, it only exists in the neutral state and electron capture behavior cannot occur. On the other hand, the formation energy of V_{Nb}^{0} is found to equal to that of V_{Li}^{4+} when $E_F = 1.75$ eV, at which point the Nb sites begin to be increasingly occupied by V dopant as the V doping concentration increases. Overall, the defect formation energies of stable V_{Li} and V_{Nb} are all found to be lower than those of the stable intrinsic Nb_{Li}^{4+} and Vac_{Li}^{-} defects. These results demonstrate that both V_{Li} and V_{Nb} can coexist in $LiNbO_3$ with dominant point defects. This could be treated as the criterion for constructing charge-compensated defect cluster models.

B. Doping-induced lattice distortion

In order to better understand the negative *U* effect of V_{Li}, we investigated the localized structural relaxations of V_{Li}^{4+}, V_{Li}^{3+}, and V_{Li}^{2+}, and compared the results to those of Nb_{Li}. From Fig. 3(b) it can be seen that the introduction of V leads to significant shrinkage of the oxygen octahedron, and that the V-O bond length decreases from 2.25 to 2.04 Å, and from 2.03 to 1.75 Å, because of the substantially stronger covalent bond of V-O as compared to Li-O. The

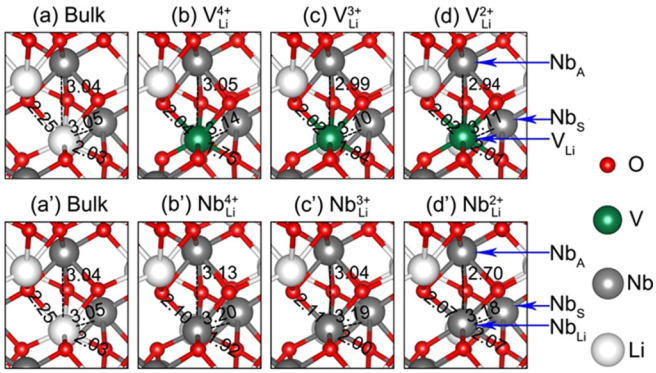

FIG. 3. Comparison between the local lattice distortions of V_{Li} (b)–(d) and Nb_{Li} (b′)–(d′) and the bulk $LiNbO_3$ (a), (a′) calculated by spin-polarized HSE06. The distances between the defect and its neighboring O and Nb ions are shown (in units of Å).

distance between V and its neighboring Nb atom along the z direction (labeled as Nb_A) is also found to slightly increase. As compared to the case of Nb_{Li}^{4+}, the shrinkage of the oxygen octahedron near V_{Li}^{4+} is more significant; this is because the covalence bond of V-O is stronger than that of Nb-O as a result of the relatively closer electronegativity between V and O. Capturing one electron leads to the movement of V_{Li}^{3+} along the z direction and the oxygen octahedron only slightly expands because of the Coulomb repulsion between the trapped electrons and the electrons surrounding the O atoms [Fig. 3(c)]. The degree of the V_{Li}^{3+} movement is comparative to that of Nb_{Li}^{3+}. When capturing one additional electron, the oxygen octahedron is observed to expand because of the stronger Coulomb repulsion between the trapped electrons and O $2p$ electronic states. Because the trapped electrons mainly distribute around V and the three O atoms along the negative z direction, the V_{Li}^{2+} defect center is further pushed toward the Nb_A direction. The energy gain due to such lattice distortion influences the switching order of V_{Li}^{3+} and V_{Li}^{2+}, which is regarded as the negative U effect. However, this is not the case for Nb_{Li}. Capturing two electrons leads to a pronounced relative movement of Nb_{Li}^{2+} and Nb_A, and their distance is largely shortened by 11.18% relative to that of $Nb_{Li}^{3+} - Nb_A$. The corresponding shortening for $V_{Li}^{2+} - Nb_A$ is only 1.67%. Therefore, the pronounced lattice distortion referring to the Nb_A contributes to the negative U effect of Nb_{Li}, which is not observed in the case of V_{Li}.

C. Electronic structure

The spin-polarized partial density of states (PDOS) of V-doped $LiNbO_3$ are shown in Fig. 4. The charge density differences between supercells with and without defects are also plotted in Fig. 4 to illustrate the doping-induced charge redistribution. The formation of most stable V_{Li}^{4+} (total spin $S = 0$) introduces unoccupied $3d$ states at approximately 1.0 eV below the CBM. The isolated impurity state is mainly attributed to the V $3d$ and O $2p$ states, and this can be confirmed via analysis of the PDOS and charge density difference maps shown in Fig. 4(b). By simultaneously trapping two electrons to form a V_{Li}^{2+} defect, two spin-parallel empty impurity states are filled as the $3d^2$ electronic

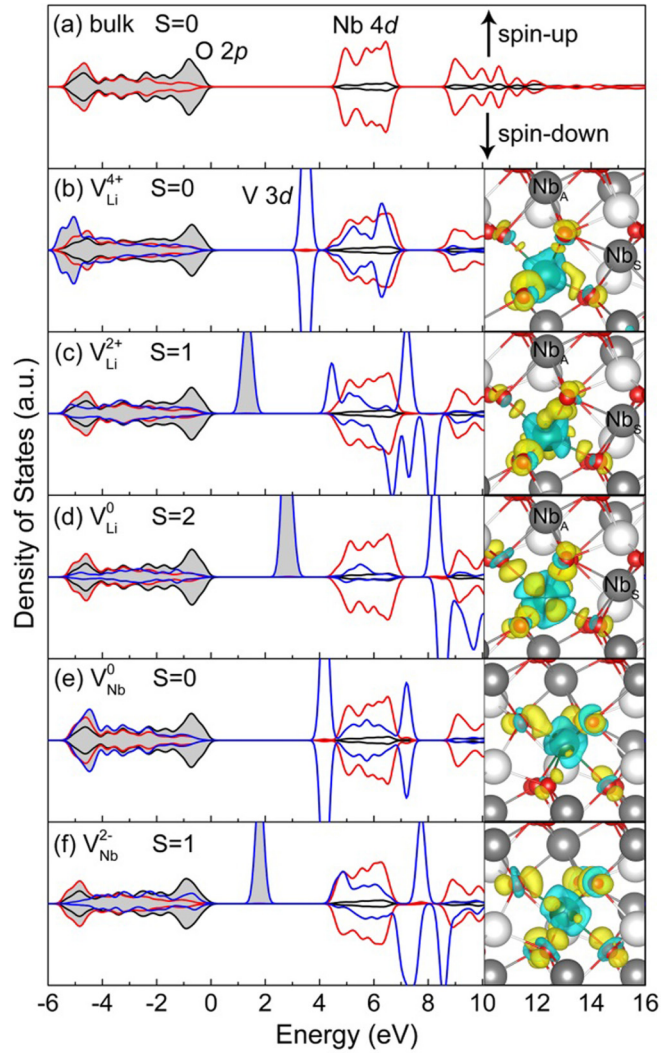

FIG. 4. Spin-polarized PDOSs and charge density differences of the bulk $LiNbO_3$ (a) and the materials with V_{Li} (b)-(d) and V_{Nb} (e)-(f) dopants within HSE06. The shadowed and blank regions represent the occupied and unoccupied states of the electron respectively. The total spins S are indicated for all the charge states. The yellow and blue regions in the charge density difference maps represent the electron accumulation and depletion, respectively.

configuration, and locate at 1.45 eV above the VBM. Therefore, the V_{Li}^{2+} defect is stable at the high-spin state with total spin $S = 1$. The charge density difference map shows that the two captured electrons are distributed around the neighboring O atoms of V_{Li}^{2+}. In order to elucidate the electronic contribution of its neighboring Nb atoms, we plot the PDOS of the V_{Li} defects and the neighboring Nb_A and Nb_s atoms in Fig. 5. Nb_s corresponds to the neighboring Nb atoms in the nonpolarization direction. Combined analysis of Figs. 4 and 5 reveals that the formation of V_{Li}^{2+} only induces lattice relaxation for the first-next-neighbor O atoms, and that there is no electronic interaction between V_{Li}^{2+} and any neighboring Nb atoms. These characteristics are typical of small bound polaron. These results are in contrast to those for Nb_{Li}, which demonstrate that the two captured electrons are distributed around the Nb_{Li}^{2+} defect and its neighboring Nb_A ion, and that

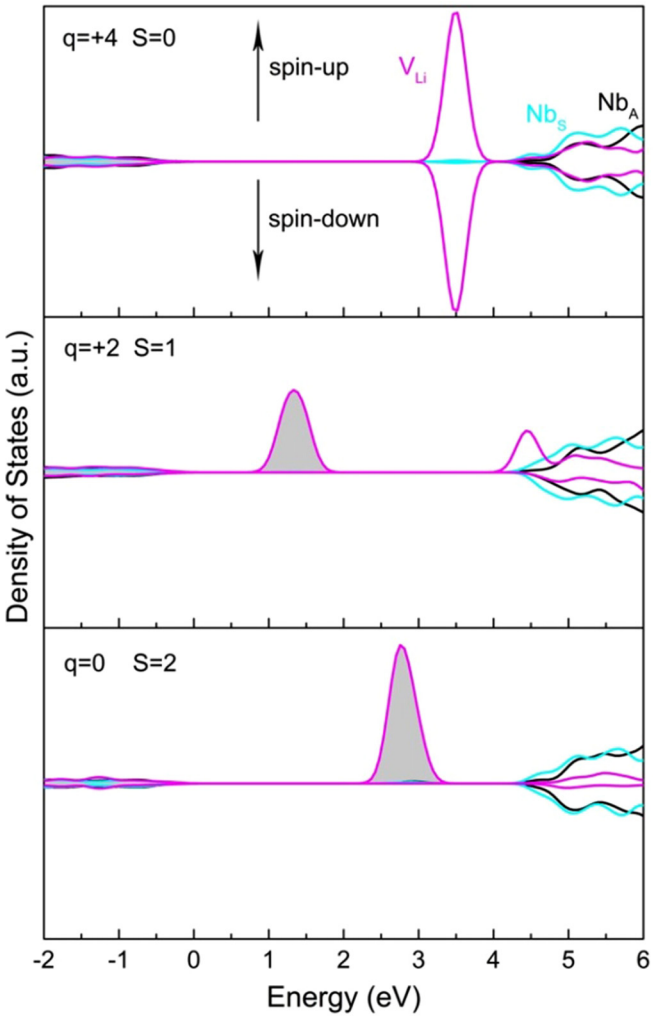

FIG. 5. Spin-polarized density of the d electronic states of V_{Li} and their neighboring Nb atoms in stoichiometric $LiNbO_3$ calculated by HSE06. The shaded and blank regions represent the occupied and unoccupied states of the electron, respectively.

Nb_{Li}^{2+} is treated as a $4d^1 - 4d^1$ bipolaron. However, although V and Nb all belong to the fifth subgroup in the periodic table of chemical elements, the photon energies associated with electron excitation from the O $2p$ states to V $3d$ states or Nb $4d$ states are distinguishable because the impurity states of V_{Li} in the band gap are all deeper than those of Nb_{Li}. The small bound polaron introduced via V doping is able to act as the $V_{Li}^{4+/2+}$ photorefractive center, which serves as a contributer to the photorefractive effect of $LiNbO_3$. Similar small bound polaron behavior is observed when V_{Li}^{2+} captures two additional electrons to form a neutral V_{Li} defect ($S = 2$), as is shown in Fig. 4(d). No electronic interaction between V_{Li}^{0} and any neighboring Nb atoms can be found from the charge density difference map in Fig. 4, and this phenomenon can further be confirmed by observing Fig. 5. However, the formation of V_{Li}^{0} is complicated by the extremely high formation energy, and thus only formed in the n-type $LiNbO_3$ samples.

The formation of V_{Nb}^{0} defect ($S = 0$) also introduces empty impurity states that are below the CBM by approximately 0.7 eV, as is shown in Fig. 4(e). By simultaneously trapping two electrons, two spin-parallel empty impurity states are filled as the $3d^2$ electronic configuration, and locate at 1.92 eV above the VBM. The V_{Nb}^{2-} defect is also stable at the high-spin state with the total spin $S = 1$. However, according to our calculation results for formation energies, the transfer from V_{Nb}^{0} to V_{Nb}^{2-} only occurs in the n-type $LiNbO_3$ crystals, indicating that the neutral V_{Nb} is unable to act as a polaron in the realistic samples.

D. Defect pairs and defect clusters

From the above analysis, we confirm that V_{Li} and Nb_{Li} are able to coexist in the $LiNbO_3$ crystal, and that they are all able to capture electrons to form polarons. So, how would the electrons distribute if V_{Li} and Nb_{Li} coexist in the $LiNbO_3$ lattice? To answer this question, we construct a model with both defects in the same supercell, and investigate the properties of the electronic structure. In general, stable V_{Li}^{4+} and Nb_{Li}^{4+} prefer to be separated because of the huge Coulombic repulsion of the same highly positive charges that they carry. This is confirmed through analysis of the calculated binding energies of the defect pairs, as is shown in Fig. 6. The binding energies of $V_{Li}^{4+} - Nb_{Li}^{4+}$ are found to be positive, and to decrease with increased distance. Therefore, we separate these two defects in the supercell to prevent interaction.

The local structures and charge density differences between the supercells with and without defect pairs are plotted in Fig. 7 in order to study the electron distributions when the $V_{Li}^{4+} - Nb_{Li}^{4+}$ pair captures electrons. It can be seen that the two stable single defects in the defect pair exhibit a local lattice distortion that is similar to that of the isolated defects. For instance, the shrinkage of the oxygen octahedron related to V_{Li}^{4+} is more significant than that related to Nb_{Li}^{4+}. After two electrons are captured, the trapped electrons are found to accumulate around V_{Li}, and this results in a larger local lattice distortion for V_{Li} than Nb_{Li}. In order to further understand the distribution of the captured electrons, we plot the PDOS of the defects and their adjacent Nb atoms in congruent $LiNbO_3$, which includes the antisite Nb_{Li}, as is shown in Fig. 8. It can be seen that, as a result of capturing two electrons, the defect state of V_{Li} is redshifted by approximately 1 eV because of the electron occupation; moreover, the $4d$ state of Nb_{Li} remains unchanged [Fig. 8(a)], indicating that the two captured electrons all positioned themselves around the V_{Li} defect. Further investigating the electron distribution around the V_{Li} defect reveals the clear contribution of the Nb_s $4d$ state to the isolated defect state in the band gap [$q = +2$, Fig. 8(a)], which is absent before the electrons are captured [$q = +4$, Fig. 8(a)]. These results demonstrate that V_{Li}^{2+} corresponds to the lattice relaxation and electron distribution around the $V_{Li} - Nb_s$ defect pair, and thus can be treated as a bipolaron. Interestingly, V_{Li}^{2+} is found to exhibit varying polaronic behavior, i.e., a small bound polaron in stoichiometric $LiNbO_3$ and a bound bipolaron in congruent $LiNbO_3$. The calculated results show that V_{Li} has stronger electron capture ability than Nb_{Li}, and that the polaronic behavior of Nb_{Li} corresponding to the $Nb_{Li} - Nb_A$ [Fig. 8(b)] could thus be moderately suppressed. When capturing two additional electrons, the captured electrons are distributed around both Nb_s and Nb_A ions, forming $V_{Li} - Nb_s$ and $V_{Li} - Nb_A$ bipolarons

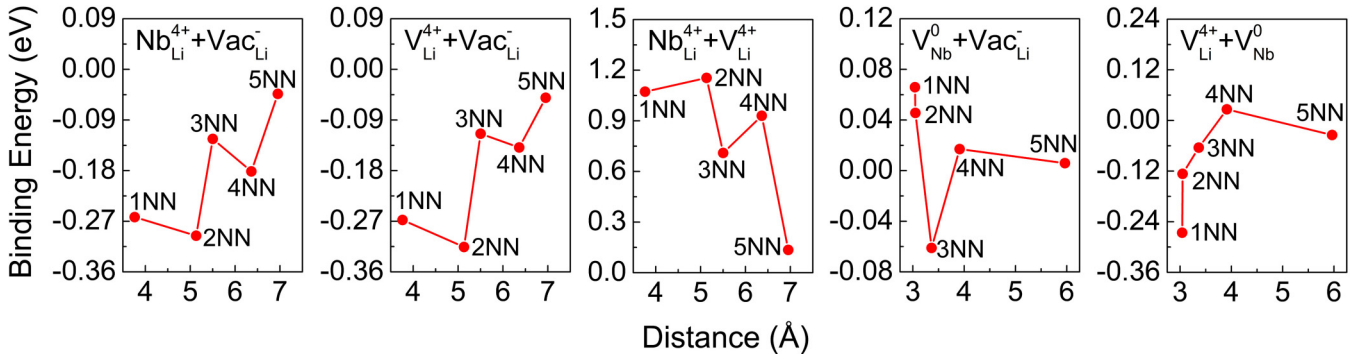

FIG. 6. Calculated binding energies of defect pairs within DFT-PBE as a function of the distance. The Fermi energy is assumed to be the VBM. The range of 1NN to 5NN corresponds to the first- to fifth-next-neighboring sites of the highly charged defect.

in the nonpolarization and polarization directions. Obviously, V_{Li}^{0} exhibits quite different polaronic behaviors in congruent and stoichiometric $LiNbO_3$. This phenomenon can be directly observed and confirmed through analysis of the charge density differences [Fig. 7(c)] and PDOS [Fig. 8(a)].

In realistic congruent $LiNbO_3$ crystals, there are numerous intrinsic Nb_{Li} and Vac_{Li} defects. These defects can charge compensate with the V dopant to form neutral defect clusters, and thus influence the electronic structures of V-doped congruent $LiNbO_3$. According to the experimental results, the doping ions prefer to first occupy the Nb_{Li} site at the lower doping concentration. In this case, all of the V_{Li}^{4+} and Nb_{Li}^{4+} defects can be compensated by the Li vacancies, i.e., the $V_{Li}^{4+}+Nb_{Li}^{4+}+8Vac_{Li}^{-}$ defect cluster. With the increase of V-doping concentration, the Nb_{Li} disappear and the dopant prefers to occupy the normal Li site. In this case, the defect cluster should be $V_{Li}^{4+}+4Vac_{Li}^{-}$. Further increase of the V-doping concentration will lead to occupation of the Nb site. In this case, the $V_{Li}^{4+}+4Vac_{Li}^{-}+V_{Nb}^{0}$ defect cluster model is more suitable. Considering that there are too many possible configurations for these three defect cluster models for all of them to be calculated, we construct the defect cluster models step by step according to the binding ability between defect pairs (Fig. 6). Taking the smallest cluster $V_{Li}^{4+}+4Vac_{Li}^{-}$ as an example, since the binding energies of the $V_{Li}^{4+}-Vac_{Li}^{-}$ pair at first- and second-next-neighboring (1NN and 2NN) sites are the highest (i.e., most negative), we position four Vac_{Li}^{-} at all possible 1NN and 2NN sites of V_{Li}^{4+}. It is found that three Vac_{Li}^{-} prefer to be positioned at the 1NN site of V_{Li}^{4+}, and that the remaining Vac_{Li}^{-} prefers to be positioned at the 2NN site, as is shown in Fig. 9(b). In our previous work [22], we obtained the most stable configuration of the $Nb_{Li}^{4+}+4Vac_{Li}^{-}$ defect cluster. As the binding ability of $V_{Li}^{4+}-Vac_{Li}^{-}$ and $Nb_{Li}^{4+}-Vac_{Li}^{-}$ is quite similar, we are able to treat the $V_{Li}^{4+}+Nb_{Li}^{4+}+8Vac_{Li}^{-}$ defect cluster as $[V_{Li}^{4+}+4Vac_{Li}^{-}]+[Nb_{Li}^{4+}+4Vac_{Li}^{-}]$. Therefore, this defect cluster model is constructed after a search for the most stable combination of the stable $V_{Li}^{4+}+4Vac_{Li}^{-}$ and $Nb_{Li}^{4+}+4Vac_{Li}^{-}$ clusters that entailed positioning the V_{Li}^{4+} at the 1NN and 2NN sites of the Vac_{Li}^{-} in the $Nb_{Li}^{4+}+4Vac_{Li}^{-}$ cluster. The most stable configuration of the

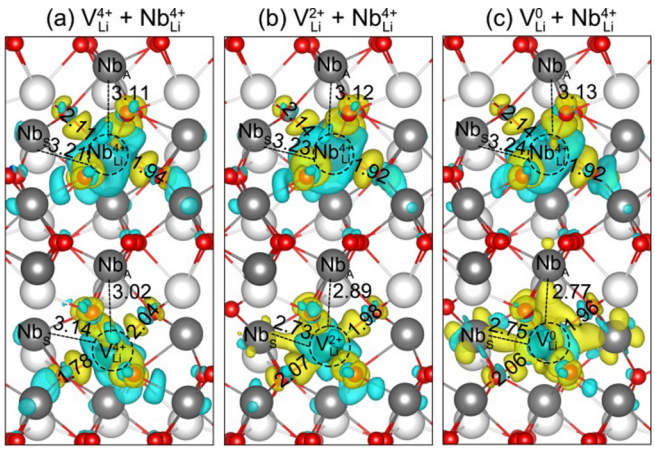

FIG. 7. Local structures and charge density difference maps of $V_{Li}^{4+}+Nb_{Li}^{4+}$(a), $V_{Li}^{2+}+Nb_{Li}^{4+}$(b) and $V_{Li}^{0}+Nb_{Li}^{4+}$(c) defect pairs within HSE06. The yellow and blue regions represent the electron accumulation and depletion, respectively. The distances labeled in the figures are in units of Å.

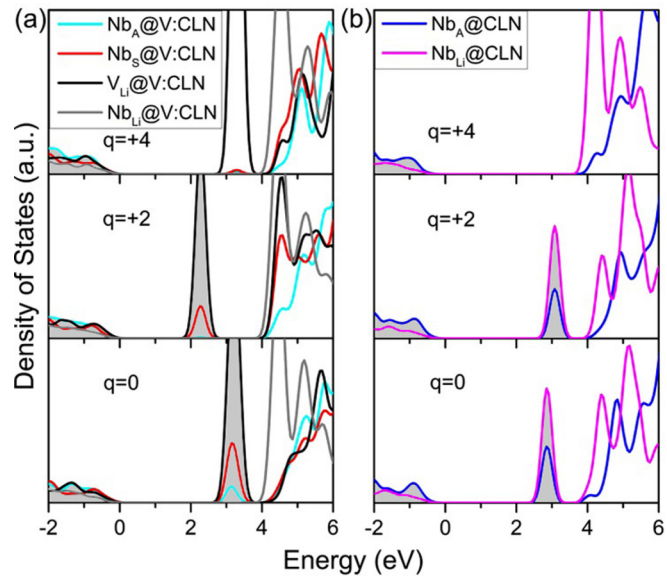

FIG. 8. Density of the *d* electronic states of charged V_{Li} and Nb_{Li} defects and their neighboring Nb (Nb_A and Nb_s) atoms in (a) V-doped congruent $LiNbO_3$ (V:CLN) and (b) undoped congruent $LiNbO_3$ (CLN) within HSE06. The shaded region represents the occupied states of the electron.

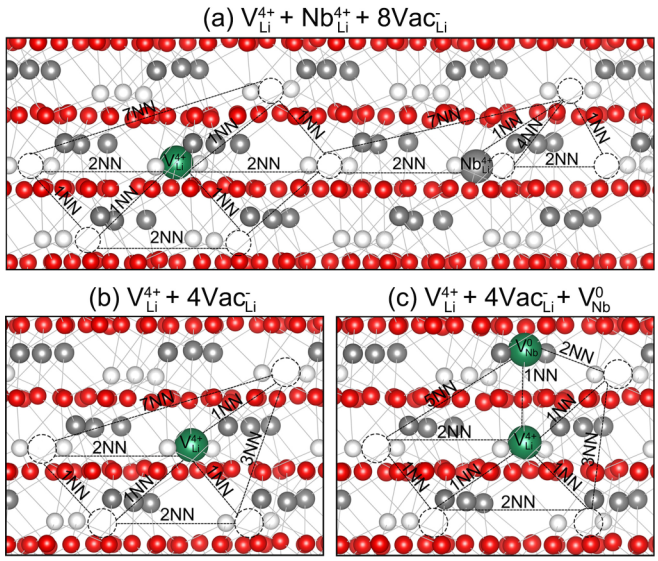

FIG. 9. Side view of the configurations of the three most stable charge-compensated defect clusters: (a) $V_{Li}^{4+} + Nb_{Li}^{4+} + 8Vac_{Li}^{-}$, (b) $V_{Li}^{4+} + 4Vac_{Li}^{-}$, and (c) $V_{Li}^{4+} + 4Vac_{Li}^{-} + V_{Nb}^{0}$. The white dotted circles represent lithium vacancies.

$V_{Li}^{4+} + Nb_{Li}^{4+} + 8Vac_{Li}^{-}$ defect cluster is shown in Fig. 9(a). We can see that V_{Li}^{4+} and Nb_{Li}^{4+} prefer to be positioned along the same xy plane. Then, we construct the $V_{Li}^{4+} + 4Vac_{Li}^{-} + V_{Nb}^{0}$ defect cluster model by positioning one V_{Nb}^{0} at the 3NN site of Vac_{Li}^{-} and the 1NN site of V_{Li}^{4+} (V_{Li}^{4+} in $V_{Li}^{4+} + 4Vac_{Li}^{-}$) according to the binding energies of $V_{Li}^{4+} + V_{Nb}^{0}$ and $Vac_{Li} + V_{Nb}^{0}$. By comparison, we found that the cluster configuration is most stable when V_{Nb}^{0} is located at the 1NN site of V_{Li}^{4+}. The maximum size of these considered defect clusters is found to be approximately 2 nm.

Here, we focus on to the electronic structures of these defect clusters. As these defect clusters are all constructed in 540-atom supercells, it would be too computationally expensive to perform the PDOS calculations by using the hybrid DFT. Thus, all of the PDOS results related to the charge-compensated defect clusters are obtained by utilizing DFT-PBE. In order to evaluate the error caused by the local functional, we first compare the PDOS of V_{Li}^{4+} calculated by HSE06 and DFT-PBE. As is shown in Fig. 10, the HSE06 and DFT-PBE functionals demonstrate similar electronic contributions of the atoms within the range of the valence band to the conduction band. Although the band gaps estimated by HSE06 and DFT-PBE are different, the respective positions of the empty defect state related to the CBM are nearly the same. Therefore, the results calculated by DFT-PBE could reflect the main characters of the defect electronic structures. By summarizing the PDOSs of the three defect clusters (Fig. 10), we get that the Vac_{Li}^{-} defects only slightly blueshift the V_{Li} defect state in the band gap via lattice relaxation, and that Nb_{Li}^{4+} decreases the band gap by introducing empty Nb 4d states just below the CBM. The neutral V_{Nb} defect also introduces the defect state below the CBM. However, this defect state is pushed toward the CBM as a result of the repulsion from the 3d states of V_{Li}. Therefore, although the formation of defect clusters yields little effect on the electronic properties

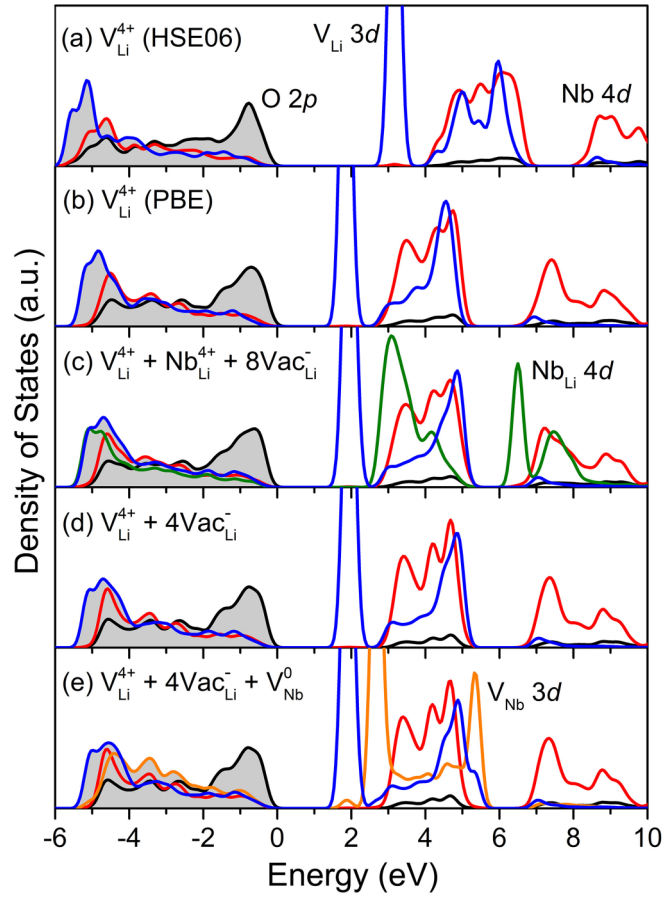

FIG. 10. PDOSs of V_{Li}^{4+} calculated by HSE06 (a) and DFT-PBE (b), respectively, and the $V_{Li}^{4+} + Nb_{Li}^{4+} + 8Vac_{Li}$ (c), $V_{Li}^{4+} + 4Vac_{Li}$ (d), $V_{Li}^{4+} + 4Vac_{Li} + V_{Nb}^{0}$ (e) defect clusters calculated by DFT-PBE.

of V_{Li} defect states in the band gap, it significantly influences the electronic character of the CBM, especially with respect to the clusters containing Nb_{Li}^{4+} and V_{Nb}^{0}. From this perspective, the differences in the electron trapping and excitation behaviors, in addition to optical properties such as the photorefractivity of V-doped stoichiometric and congruent $LiNbO_3$ can be primarily attributed to the change of the CBM and the additional V_{Nb}^{0} impurity state that is introduced as a result of increasing the V doping concentration.

IV. CONCLUSION

In summary, the microscopic properties of V-doped $LiNbO_3$, including the doping configurations, relative stability, electronic structures, and its interaction with the intrinsic point defects, are investigated by using the spin-polarized (semi)local and hybrid density functional theories. The calculated defect formation energies show that V prefers to substitute Li at its highest +4 charge state, and that it could substitute Nb to form a neutral V_{Nb} defect as a result of the Fermi level being increased. The most stable V_{Li}^{4+} is able to simultaneously capture two electrons to form a V_{Li}^{2+} small bound polaron in stoichiometric $LiNbO_3$, while a $V_{Li} - Nb_s$ bound bipolaron in the congruent samples. In congruent $LiNbO_3$, V_{Li}^{4+} demonstrates a stronger ability to trap electrons than the intrinsic defect Nb_{Li}^{4+}. We are also able to observe

both $V_{Li} - Nb_s$ and $V_{Li} - Nb_A$ bound bipolarons if under the condition that additional electrons are captured to form a neutral V_{Li} defect. In addition, the formation of the charge-compensated defect clusters is also found to significantly influence the electronic characters of the CBM, which thus causes the doping-induced electronic and optical properties in stoichiometric and congruent $LiNbO_3$ to vary.

ACKNOWLEDGMENTS

We gratefully acknowledge the financial support from the National Natural Science Foundation of China (No. 51502158) and the Opening Foundation of State Key Laboratory of Crystal Materials at Shandong University (No. ZPY-2018-15).

[1] A. Ballman, J. Amer. Ceram. Soc. **48**, 112 (1965).
[2] K. K. Wong, *Properties of Lithium Niobate*, *INSPEC* (IET, Stevenage, UK, 2002).
[3] G. D. Boyd, K. Nassau, R. C. Miller, W. L. Bond, and A. Savage, Appl. Phys. Lett. **5**, 234 (1964).
[4] F. S. Chen, J. Appl. Phys. **40**, 3389 (1969).
[5] V. Gopalan, V. Dierolf, and D. A. Scrymgeour, Annu. Rev. Mater. Res. **37**, 449 (2007).
[6] Y. Dong, S. Liu, W. Li, Y. Kong, S. Chen, and J. Xu, Opt. Lett. **36**, 1779 (2011).
[7] Y. Dong, S. Liu, Y. Kong, S. Chen, R. Rupp, and J. Xu, Opt. Lett. **37**, 1841 (2012).
[8] W. G. Schmidt, M. Albrecht, S. Wippermann, S. Blankenburg, E. Rauls, F. Fuchs, C. Rödl, J. Furthmüller, and A. Hermann, Phys. Rev. B **77**, 035106 (2008).
[9] A. Sanson, A. Zaltron, N. Argiolas, C. Sada, M. Bazzan, W. G. Schmidt, and S. Sanna, Phys. Rev. B **91**, 094109 (2015).
[10] D. A. Bryan, R. Gerson, and H. E. Tomaschke, Appl. Phys. Lett. **44**, 847 (1984).
[11] H. Qiao, J. Xu, G. Zhang, X. Zhang, Q. Sun, and G. Zhang, Phys. Rev. B **70**, 094101 (2004).
[12] W. Phillips, D. L. Staebler, and J. J. Amodei, RCA Rev. **33**, 94 (1972).
[13] D. K. Mcmillen, T. D. Hudson, J. Wagner, and J. Singleton, Opt. Express **2**, 491 (1998).
[14] O. F. Schirmer, M. Imlau, C. Merschjann, and B. Schoke, J. Phys.: Condens. Matter **21**, 123201 (2009).
[15] Y. Li, W. G. Schmidt, and S. Sanna, Phys. Rev. B **89**, 094111 (2014).
[16] H. H. Nahm and C. H. Park, Phys. Rev. B **78**, 184108 (2008).
[17] H. L. Wang, Y. Hang, J. Xu, L. H. Zhang, S. N. Zhu, and Y. Y. Zhu, Mater. Lett. **58**, 3119 (2004).
[18] S. Erdei and V. T. Gabrieljan, Cryst. Res. Technol. **24**, 987 (1989).
[19] K. Kitamura, J. K. Yamamoto, N. Iyi, S. Kimura, and T. Hayashi, J. Cryst. Growth **116**, 327 (1992).
[20] K. Kitamura, Y. Furukawa, K. Niwa, V. Gopalan, and T. E. Mitchell, Appl. Phys. Lett. **73**, 3073 (1998).
[21] F. P. Safaryan, R. S. Feigelson, and A. M. Petrosyan, J. Appl. Phys. **85**, 8079 (1999).
[22] Y. Li, W. G. Schmidt, and S. Sanna, Phys. Rev. B **91**, 174106 (2015).
[23] D. M. Smyth, Prog. Solid State Chem. **15**, 145 (1984).
[24] S. C. Abrahams and P. Marsh, Acta Crystallogr. Sect. B **42**, 61 (1986).
[25] H. Donnerberg, S. M. Tomlinson, C. R. A. Catlow, and O. F. Schirmer, Phys. Rev. B **40**, 11909 (1989).
[26] P. Hohenberg and W. Kohn, Phys. Rev. **136**, B864 (1964).
[27] W. Kohn and L. J. Sham, Phys. Rev. **140**, A1133 (1965).
[28] F. Bechstedt, *Quasiparticle Corrections for Energy Gaps in Semiconductors*, Advances in Solid State Physics, Vol. 32 (Springer, Berlin, 1992).
[29] A. Alkauskas and A. Pasquarello, Phys. Rev. B **84**, 125206 (2011).
[30] L. S. dos Santos, W. G. Schmidt, and E. Rauls, Phys. Rev. B **84**115201 (2011).
[31] J. Hafner, J. Comput. Chem. **29**, 2044 (2008).
[32] M. Cococcioni and S. de Gironcoli, Phys. Rev. B **71**, 035105 (2005).
[33] J. Heyd, G. E. Scuseria, and M. Ernzerhof, J. Chem. Phys. **118**, 8207 (2003).
[34] A. V. Krukau, O. A. Vydrov, A. F. Izmaylov, and G. E. Scuseria, J. Chem. Phys. **125**, 224106 (2006).
[35] G. Kresse and J. Furthmüller, Comput. Mater. Sci. **6**, 15 (1996).
[36] G. Kresse and J. Furthmüller, Phys. Rev. B **54**, 11169 (1996).
[37] G. Kresse and D. Joubert, Phys. Rev. B **59**, 1758 (1999).
[38] J. P. Perdew, K. Burke, and M. Ernzerhof, Phys. Rev. Lett. **77**, 3865 (1996).
[39] H. J. Monkhorst and J. D. Pack, Phys. Rev. B **13**, 5188 (1976).
[40] G. C. Van de Walle and J. Neugebauer, J. Appl. Phys. **95**, 3851 (2004).
[41] S. Lany and A. Zunger, Phys. Rev. B **78**, 235104 (2008).
[42] H. P. Komsa, T. T. Rantala, and A. Pasquarello, Phys. Rev. B **86**, 045112 (2012).
[43] G. Makov and M. C. Payne, Phys. Rev. B **51**, 4014 (1995).
[44] C. Freysoldt, J. Neugebauer, and C. G. Van de Walle, Phys. Rev. Lett. **102**, 016402 (2009).
[45] W. R. L. Lambrecht, Phys. Status Solidi B **248**, 1547 (2011).
[46] U. Gerstmann, P. Deak, R. Rurali, B. Aradi, T. Frauenheim, and H. Overhof, Phys. B: Condens. Matter **340–342**, 190 (2003).
[47] A. Savage, J. Appl. Phys. **37**, 3071 (1966).
[48] H. Xu, D. Lee, J. He, S. B. Sinnott, V. Gopalan, V. Dierolf, and S. R. Phillpot, Phys. Rev. B **78**, 174103 (2008).
[49] P. W. Anderson, Phys. Rev. Lett. **34**, 953 (1975).
[50] S. Sanna and W. G. Schmidt, Phys. Rev. B **81**, 214116 (2010).